Dalton Transactions

PAPER

View Article Online
View Journal

Cite this: DOI: 10.1039/d6dt01134a

Porous Ni-based metal–organic frameworks reduce the oxygen evolution temperature of lithium perchlorate

Nicholas A. Tomalia, [a] Yulia Rakova, [a] Ashley N. Tubman [a] and Adam J. Matzger *[a,b]

Received 12th May 2026,
Accepted 20th May 2026

DOI: 10.1039/d6dt01134a

rsc.li/dalton

The temperature at which inorganic oxidizers evolve oxygen is a key operational constraint in applications ranging from energetic materials to chemical oxygen generators and life-support systems. However, commonly used chlorates and perchlorates typically decompose at temperatures exceeding 400 °C, imposing limitations on efficiency, thermal management, and materials compatibility and motivating strategies for lower-temperature oxygen release without sacrificing yield. Here, porous Ni-based metal–organic frameworks catalyze $LiClO_4$ decomposition, lowering oxygen evolution onset temperatures by up to 180 °C relative to pure $LiClO_4$ while preserving >95 mol% O_2 yield. Framework porosity enables oxidizer melt-infiltration and promotes intimate nanoscale oxidizer-catalyst contact, enhancing catalytic effectiveness relative to the most effective nonporous Ni catalyst identified through Ni-salt screening. This approach demonstrates how framework porosity can be leveraged to enhance oxidizer-catalyst interactions and improve catalytic efficiency in oxygen-generating systems through structural design rather than solely through metal identity or loading, enabling lower-temperature oxygen release without compromising oxygen yield.

Introduction

Oxygen generation from decomposing oxidizing salts is critical to a wide range of technologies that rely on self-contained oxidation; energetic materials (EMs; including propellants, pyrotechnics, and explosives) rely on *in situ* oxygen release to control reaction rate,[1,2] heat output,[3–5] and gas/pressure evolution.[6–12] Controlled oxygen evolution is also essential for chemical oxygen generators[13–15] and life-support safety systems used in aircraft, submarines, spacecraft, and mine rescue equipment,[16–18] where reliable oxygen delivery is required in sealed or oxygen-deficient environments.[19] As such, strategies that lower oxidizer decomposition temperature while preserving oxygen yield are desirable.

We have recently demonstrated that metal–organic frameworks (MOFs) can react with the melt of lithium perchlorate ($LiClO_4$; melting point: 247 °C) to make explosives and that the temperature at which these EMs decompose indicates that the MOFs are catalysing availability of oxygen from perchlorate at a much lower temperature than pure perchlorate decomposition.[20,21] While the catalytic decomposition of ammonium perchlorate (AP) has been studied extensively using metal oxides,[22–26] metal-containing composites,[27–29] MOFs,[30–33] energetic MOFs,[34,35] bimetallic MOFs,[36–38] and perovskites,[39] comparatively less is known about the catalytic decomposition of metal perchlorates. $LiClO_4$ decomposition temperatures can be lowered by approximately 100 °C relative to pure $LiClO_4$ in the presence of elemental Mn.[40] Metal oxide catalysts including Co_2O_3, MnO_2, Li_2O, and CuO have also been shown to reduce $LiClO_4$ decomposition temperatures by 70–100 °C relative to pure $LiClO_4$.[41–44] Metal composite sol–gel catalysts Cr_2–Cu and $Ce_xCu_{(1-x)}O_{(1+x)}$ achieve ~50% of the theoretical $LiClO_4$ conversion at 420 °C.[45,46] Collectively, these studies demonstrate that metal species can catalyse $LiClO_4$ decomposition; however, the influence of catalyst porosity and the role of intimate nanoscale oxidizer-catalyst contact on facilitating oxygen release at lower temperatures remains largely unexplored. To address this gap, isoreticular Ni-based MOFs with varied pore sizes are investigated here as catalysts for $LiClO_4$ decomposition. By comparing Ni-MOF-74 and UMCM-74-I(Ni), which share identical Ni^{2+} catalytic sites but differ substantially in pore dimensions, with a nonporous Ni salt ($Ni(NO_3)_2{\cdot}6H_2O$), this study isolates the influence of porosity on facilitating oxygen release of $LiClO_4$.

[a]Department of Chemistry, University of Michigan, 930 North University Avenue, Ann Arbor, Michigan 48109, USA. E-mail: matzger@umich.edu
[b]Macromolecular Science and Engineering Program, University of Michigan, Ann Arbor, Michigan 48109, USA

Experimental

Materials

Lithium perchlorate ($LiClO_4$), 99+% purity was obtained from Fisher Scientific and dried at 150 °C for 4 h. Nickel benzoate trihydrate ($Ni(OBz)_2{\cdot}3H_2O$) was synthesized according to the published procedure.[47] All other chemicals were used as received. 2,5-Dihydroxyterephthalic acid was purchased from TCI America. Methyl 2-hydroxy-4-iodobenzoate (97%) was purchased from AmBeed. Nickel nitrate hexahydrate ($Ni(NO_3)_2{\cdot}6H_2O$), *N*,*N*-dimethylformamide (DMF), methanol (MeOH), triethylamine, tetrahydrofuran (THF), methylene chloride, piperidine, sodium hydroxide, benzoic acid, and nickel oxide were purchased from Fisher Scientific. Nickel powder was purchased from Alfa Aesar. Ethanol (EtOH) was purchased from Decon Laboratories. Copper iodide, (trimethyl silyl)acetylene, copper acetate monohydrate, nickel acetate tetrahydrate, and nickel chloride hexahydrate were purchased from Aldrich. Tetrabutylammonium fluoride was purchased from Acros Organics.

Synthesis and activation of Ni-MOF-74 catalyst

Ni-MOF-74 was synthesized according to the published procedure but scaled-up four times.[48] The MOF was activated under dynamic vacuum (<0.03 Torr) at 250 °C for 12 h. The activated material was stored under an inert atmosphere.

Synthesis and activation of UMCM-74-I(Ni) catalyst

The UMCM-71-I linker and UMCM-74-I(Ni) were synthesized and the MOF was activated by following the published procedures.[21]

Powder X-ray diffraction

Room temperature PXRD measurements were carried out on a Rigaku MiniFlex 600 equipped with a $\theta/2\theta$ goniometer. Diffraction data were obtained in Bragg–Brentano geometry using Ni-filtered Cu Kα radiation ($K\alpha_1$ = 1.54059 Å, $K\alpha_2$ = 1.54441 Å, $K\alpha_1/K\alpha_2$ = 0.5) operated at 40 kV and 15 mA. The incident beam employed both a variable and fixed (1.25° divergence) slit and a 5° Soller slit, a 5° Soller slit was also positioned on the diffracted beam side. X-rays were detected using a silicon-based linear position sensitive *D*/tex Ultra2 detector operating in 1D scanning mode. Ground samples of Ni-MOF-74, $LiClO_4$, and $Ni(NO_3)_2{\cdot}6H_2O$ were packed into the depression of a silicon zero-background holder. Powder patterns were collected over a 2θ range of 5–50° 2θ with a step size of 0.01° and a scan rate of 3.0° min^{-1}. Powder patterns for $Ni(OBz)_2{\cdot}3H_2O$ were collected over a 2θ range of 4–50° 2θ with a step size of 0.01° and a scan rate of 5.0° min^{-1}. For UMCM-74-I(Ni), room temperature PXRD data were collected with a PANalytical Emprean diffractometer in Bragg–Brentano geometry using a Cu-Kα radiation tube operated at 45 kV and 40 mA. The incident beam utilized a Bragg–Brentano HD Cu X-ray optic equipped with fixed soller slits (0.04 rad) and a 10 mm fixed mask. X-ray detection was accomplished with a X'Celerator Scientific detector operated in 1-D scanning mode. Samples were finely ground to reduce preferred orientation and packed into the depression of a silicon zero-background holder. PXRD data were acquired across a 2θ range spanning 2° to 50°.

N_2 sorption

Nitrogen sorption isotherms were measured using a NOVA e-Series 4200 surface analyzer (Quantachrome Instruments) and ultra-high purity N_2 (99.999%) that was purchased from Cryogenic Gases. Isotherm measurements were performed using ~20 mg of sample which was loaded into a glass sample cell and analyzed at 77 K. Using NOVAwin software, the obtained isotherms were analyzed and Brunauer–Emmett–Teller (BET) specific surface areas were estimated. The P/P_0 range was determined using a consistency criterion plot for BET surface area analysis.

Thermogravimetric analysis-mass spectrometry (TGA-MS)

TGA-MS experiments were performed on a TA Instruments Discovery TGA 5500, calibrated with an Alumel standard, with TRIOS Thermal analysis software (version V5.7). A Hiden Analytical HPR-20 QIC mass spectrometer with MASsoft 10 (version 10.37.0.7) was coupled to the TGA furnace exhaust *via* a heated quartz inert capillary transfer line (~3.2 mL min^{-1} sampling rate) maintained at 160 °C. The MS was operated in Multiple Ion Detection (MID) mode using a Faraday cup detector with an ionization energy of 70 eV to enable real-time monitoring of discrete *m*/*z* channels. For $Ni(NO_3)_2{\cdot}6H_2O$ and $LiClO_4/Ni(NO_3)_2{\cdot}6H_2O$ mixtures *m*/*z* 18, 30, 32, 44, and 46 amu corresponding to H_2O, NO, O_2, N_2O, and NO_2, respectively, were monitored. For $LiClO_4$, $LiClO_4$/Ni-MOF-74, and $LiClO_4$/UMCM-74-I(Ni) mixtures *m*/*z* 18, 28, 32, and 44 amu corresponding to H_2O, N_2/CO, O_2, and CO_2, respectively, were monitored. TGA and MS data acquisition were synchronized using a hardware Start/Stop trigger initiated at the beginning of the TGA temperature program. Samples were removed from a nitrogen-filled glovebox, loaded into platinum sample pans and heated to 600 °C under ultra-high purity helium (99.999%) at a purge flow rate of 25 mL min^{-1}. Decomposition onset temperatures were determined using the "onset tool" in the TRIOS software by selecting a temperature point at which sample mass remained constant prior to the weight loss event associated with decomposition and a second higher-temperature point corresponding to rapid mass loss. From each of the temperature points, a tangent line is drawn, and the point at which they intersect is determined as the decomposition onset temperature. The decomposition midpoint was determined by identifying the temperatures at which mass remained constant before and after the weight loss event associated with decomposition and calculating the midpoint between these temperatures. The decomposition completion temperature is determined as the first point at which sample weight remains constant following the weight loss corresponding to decomposition. Gaseous decomposition products were quantified by integrating the corresponding *m*/*z* signals and normalizing peak areas using Relative Sensitivity Factors obtained from the Hiden library in MASsoft 10.

Results and discussion

UMCM-74-I(Ni) is an isoreticular (same network topology with lattice parameters increasing alongside linker length) analogue

of Ni-MOF-74 in which the coordinating *o*-hydroxycarboxylate is appended to a bisphenyl diyne core, resulting in dramatic linker extension and pore expansion with minimal steric obstruction of the pores (Fig. 1).[21] Consequently, UMCM-74-I (Ni) exhibits a pore diameter of 3.0 nm and pore volume of 1.50 $cm^3\ g^{-1}$, whereas Ni-MOF-74 exhibits a pore diameter of 1.5 nm and pore volume of 0.58 $cm^3\ g^{-1}$. We hypothesize that the porosity and the ability of the MOFs to accommodate oxidizer melt-infiltration will facilitate intimate nanoscale oxidizer-catalyst contact, thereby enhancing catalytic effectiveness and reducing the $LiClO_4$ oxygen release temperature.

To select the most effective nonporous control catalyst for comparison with the porous Ni-MOF catalysts, five Ni-salts and Ni powder were evaluated to identify the nonporous Ni catalyst that imparts the greatest reduction in the decomposition temperature of $LiClO_4$. Physical mixtures of $LiClO_4$ and each nonporous catalyst (~0.42 wt% Ni relative to composite, selected to match the Ni content in a 2 wt% $Ni(NO_3)_2{\cdot}6H_2O$ mixture) were homogenized using a mortar and pestle in a nitrogen-filled glovebox. The thermal decomposition of each $LiClO_4$/catalyst mixture was evaluated by thermogravimetric analysis (TGA) and compared to pure $LiClO_4$. All samples exhibited initial weight loss associated with dehydration. Among the salts evaluated, $Ni(NO_3)_2{\cdot}6H_2O$ most effectively reduced the $LiClO_4$ decomposition temperature (Fig. 2). A comparable catalytic effect was observed for $LiClO_4$ with $Ni(OAc)_2{\cdot}4H_2O$. However, because acetate introduces additional carbon and lower oxygen content relative to nitrate, which would negatively impact oxygen yield in subsequent studies, $Ni(NO_3)_2{\cdot}6H_2O$ was selected as the Ni catalyst to isolate the influence of porosity on $LiClO_4$ catalysis.

Physical mixtures of $LiClO_4$ with Ni-MOF-74, UMCM-74-I (Ni), and $Ni(NO_3)_2{\cdot}6H_2O$ were prepared by cogrinding in a nitrogen-filled glovebox using a mortar and pestle. MOF/$LiClO_4$ mixtures were formulated to match the Ni loading of a 2 wt% $Ni(NO_3)_2{\cdot}6H_2O$ addition with $LiClO_4$ (corresponding to 0.42 wt% Ni relative to composite). Thermogravimetric analysis coupled with mass spectrometry (TGA-MS) was used to determine the decomposition onset temperature, midpoint temperature (50% oxygen evolution), and completion temperature of each mixture, as well as to identify and quantify gaseous decomposition products after sample dehydration (>250 °C). TGA was used to quantify oxygen release from $LiClO_4$, while MS was used to confirm O_2 as the exclusive gaseous decomposition product. The midpoint temperature is particularly relevant from an operational standpoint, as it better represents the temperature at which the majority of oxygen evolution occurs, rather than relying solely on onset or completion temperatures to characterize oxygen release.

All samples exhibited an initial weight loss associated with salt dehydration. Anhydrous $LiClO_4$ decomposition begins at 505 °C, exhibits a midpoint at ~515 °C, and completes at

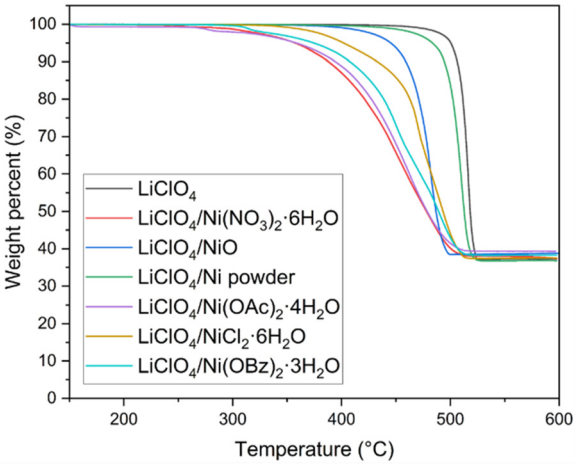

Fig. 2 TGA thermograms (10 °C min^{-1}) showing the thermal decomposition of pure $LiClO_4$ (black), $LiClO_4/Ni(NO_3)_2{\cdot}6H_2O$ (red), $LiClO_4$/NiO (blue), $LiClO_4$/Ni powder (green), $LiClO_4/Ni(OAc)_2{\cdot}4H_2O$ (purple), $LiClO_4/NiCl_2{\cdot}6H_2O$ (yellow), and $LiClO_4/Ni(OBz)_2{\cdot}3H_2O$ (light blue) mixtures after dehydration. All $LiClO_4$/catalyst mixtures contain 0.42 wt% Ni.

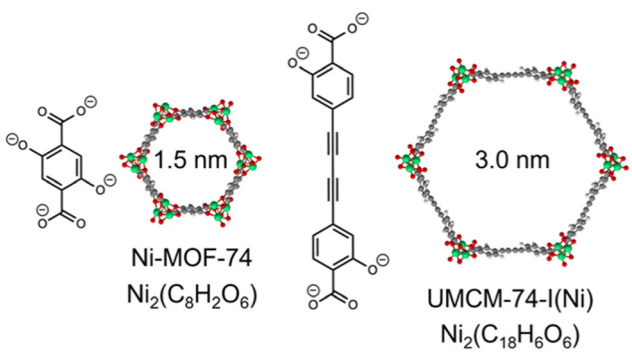

Fig. 1 Structure of a single pore in Ni-MOF-74 (left) and UMCM-74-I (Ni) (right) viewed along the *c*-axis, with corresponding linker structures and framework compositions.

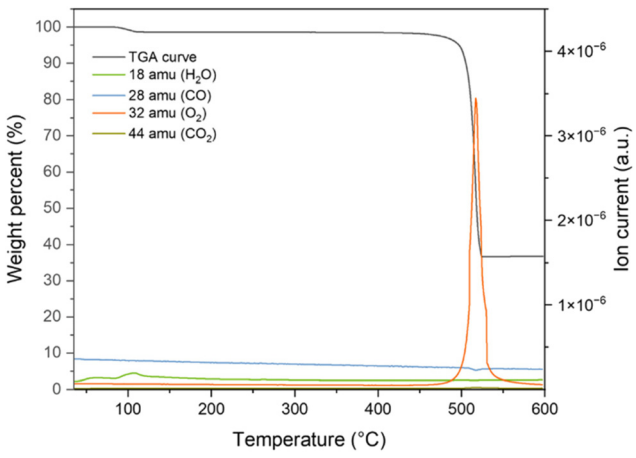

Fig. 3 TGA-MS data for $LiClO_4$ showing sample weight loss (black trace). The initial mass loss corresponds to dehydration (green trace) and the second mass loss corresponds to oxygen release (orange trace).

Table 1 Thermal decomposition (T_d) onset, midpoint, and completion temperatures collected at 10 °C min^{-1} for pure $LiClO_4$, and $LiClO_4$/Ni$(NO_3)_2{\cdot}6H_2O$, $LiClO_4$/Ni-MOF-74, and $LiClO_4$/UMCM-74-I(Ni) mixtures containing 0.42, 0.21, and 0.10 wt% Ni content

	Weight percent Ni content (%)	T_d onset (°C)	T_d midpoint (°C)	T_d completion (°C)
$LiClO_4$	0	504.6	514.6	523.8
$LiClO_4$/Ni$(NO_3)_2{\cdot}6H_2O$	0.42	373.3	444.8	511.7
$LiClO_4$/Ni-MOF-74	0.42	317.5	420.0	503.2
$LiClO_4$/UMCM-74-I(Ni)	0.42	324.1	422.6	502.3
$LiClO_4$/Ni$(NO_3)_2{\cdot}6H_2O$	0.21	385.2	484.9	516.3
$LiClO_4$/Ni-MOF-74	0.21	345.4	463.5	510.8
$LiClO_4$/UMCM-74-I(Ni)	0.21	353.9	467.1	511.2
$LiClO_4$/Ni$(NO_3)_2{\cdot}6H_2O$	0.10	450.4	487.9	517.8
$LiClO_4$/Ni-MOF-74	0.10	419.1	477.9	514.0
$LiClO_4$/UMCM-74-I(Ni)	0.10	421.9	480.2	514.4

~524 °C, with oxygen evolution corresponding to 60.1 wt% (theoretical O_2 release = 60.15 wt%) (Fig. 3).

Ni-based catalysts considerably lower the $LiClO_4$ decomposition onset, midpoint, and completion temperatures relative to pure $LiClO_4$ (Table 1). In the presence of 2 wt% Ni $(NO_3)_2{\cdot}6H_2O$ (0.42 wt% Ni), the nonporous Ni catalyst leading to the greatest reduction in decomposition temperature (see Fig. 2), $LiClO_4$ oxygen release initiates at 373 °C, representing a 132 °C temperature reduction compared to pure $LiClO_4$. The decomposition midpoint and completion temperatures occur at ~445 °C and ~512 °C, corresponding to temperature reductions of 70 °C and 12 °C, respectively, relative to pure $LiClO_4$. At identical Ni loadings (0.42 wt% Ni), both MOF-containing mixtures exhibit further reductions in decomposition temperatures relative to the nonporous Ni$(NO_3)_2{\cdot}6H_2O$ control and are significantly lower than pure $LiClO_4$ (Fig. 4a; Table 1). Oxygen release initiates at approximately 318 °C for Ni-MOF-74 and 324 °C for UMCM-74-I(Ni), ~50 °C lower in temperature than $LiClO_4$/Ni$(NO_3)_2{\cdot}6H_2O$ and ~180 °C lower than pure $LiClO_4$. $LiClO_4$/Ni-MOF-74 midpoint and completion temperatures (similar to those for $LiClO_4$/UMCM-74-I(Ni)) are reduced by ~22 °C and ~9 °C relative to $LiClO_4$/Ni$(NO_3)_2{\cdot}6H_2O$, and ~92 °C and ~21 °C relative to pure $LiClO_4$ (Table 1). Collectively, these data suggest that porous Ni-MOFs are more effective catalysts for reducing $LiClO_4$ decomposition temperature than the most effective nonporous metal salt at the same Ni content, consistent with improved nanoscale oxidizer-catalyst contact facilitated by the $LiClO_4$ melt infiltrating the MOF pores.

The effect of heating rate on $LiClO_4$ decomposition was examined at 10 °C min^{-1} and 1 °C min^{-1} for $LiClO_4$/Ni-MOF-74 and $LiClO_4$/Ni$(NO_3)_2{\cdot}6H_2O$ mixtures (Fig. 4b). Slower heating lowers decomposition onset, midpoint, and completion temperatures for both catalyzed mixtures but does not substantially change the relative differences in midpoint or completion temperatures. At 0.42 wt% Ni and 1 °C min^{-1}, $LiClO_4$/Ni-MOF-74 decomposition starts ~44 °C lower in temperature than $LiClO_4$/Ni$(NO_3)_2{\cdot}6H_2O$ (328 °C), with the midpoint 14 °C lower. Overall, onset, midpoint, and completion temperatures decrease at the slower heating rate by 34 °C, 41 °C, and 71 °C for $LiClO_4$/Ni-MOF-74, and by 52 °C, 56 °C, and 84 °C for $LiClO_4$/Ni$(NO_3)_2{\cdot}6H_2O$ compared to the 10 °C

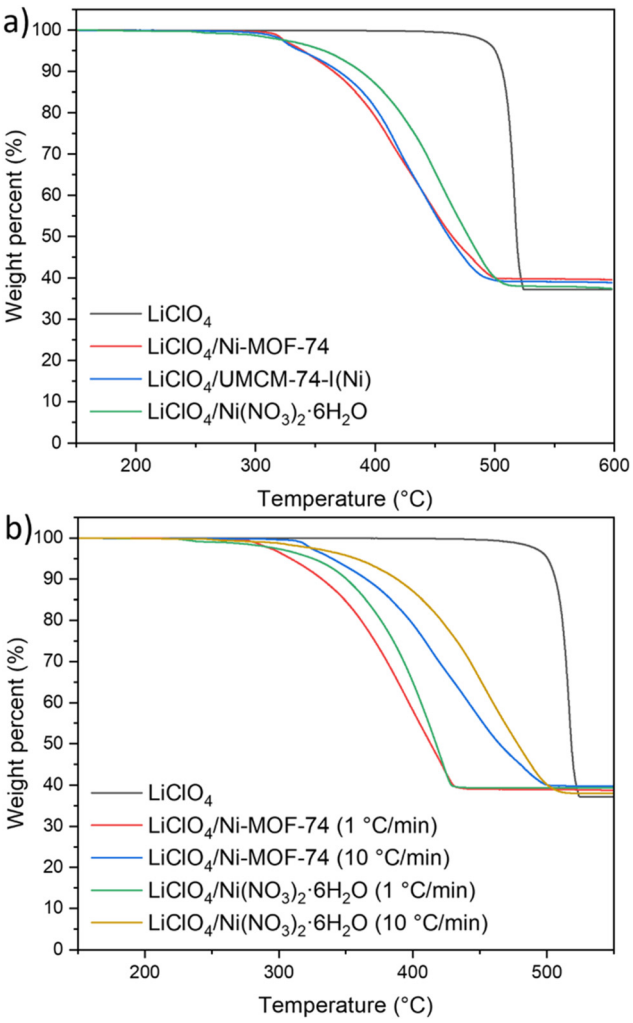

Fig. 4 (a) TGA thermograms (10 °C min^{-1}) showing the decomposition of pure $LiClO_4$ (black), $LiClO_4$/Ni-MOF-74 (red), $LiClO_4$/UMCM-74-I(Ni) (blue), and $LiClO_4$/Ni$(NO_3)_2{\cdot}6H_2O$ (green) mixtures after dehydration. (b) TGA thermograms showing the decomposition of pure $LiClO_4$ (black), $LiClO_4$/Ni-MOF-74 (red), and $LiClO_4$/Ni$(NO_3)_2{\cdot}6H_2O$ (green) heated at 1 °C min^{-1}, and $LiClO_4$/Ni-MOF-74 (blue) and $LiClO_4$/Ni$(NO_3)_2{\cdot}6H_2O$ (brown) heated at 10 °C min^{-1}. All $LiClO_4$/catalysts mixtures contain 0.42 wt% Ni.

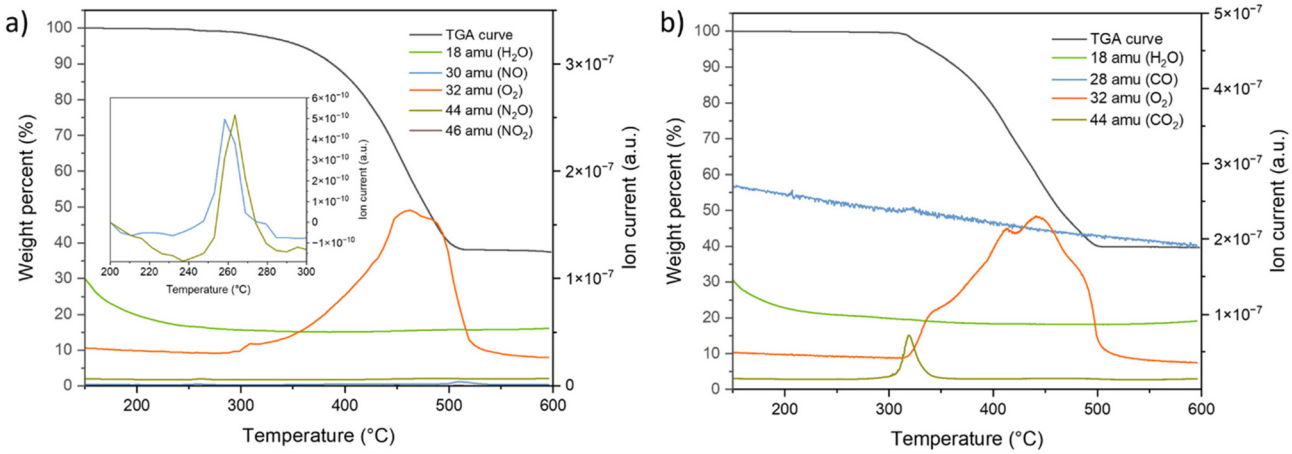

Fig. 5 TGA-MS data showing the decomposition of (a) $LiClO_4/Ni(NO_3)_2{\cdot}6H_2O$ with peaks at ~260 °C corresponding to NO and N_2O (inset) and (b) $LiClO_4$/Ni-MOF-74 mixtures containing 0.42 wt% Ni content after dehydration as well as the gaseous products detected by MS. The levels of N_2, O_2, CO_2, and H_2O are elevated due to atmospheric intrusion and therefore only increases relative to baseline levels are significant.

min^{-1} data (Fig. 4b). These results suggest that while absolute decomposition temperatures depend on heating rate, the catalytic advantage of the porous MOF over the nonporous salt is maintained across heating conditions. Bimetallic salt mixtures containing $Ni(NO_3)_2{\cdot}6H_2O$ were also explored to assess potential metal synergy, but no synergistic catalytic effect was observed (see S2 in the SI).

While the porous MOFs enable lower-temperature oxygen release from $LiClO_4$ at all catalyst loadings relative to the most effective nonporous salt catalyst, quantification of evolved gases is necessary to assess oxygen production of each mixture. Pure $LiClO_4$ decomposes to LiCl and $2O_2$, releasing 60.1 wt% oxygen (100 mol%). In the presence of Ni $(NO_3)_2{\cdot}6H_2O$ (0.42 wt% Ni content in mixture), decomposition produces primarily O_2 (98.6 mol%), with minor quantities of H_2O, NO, and N_2O[49,50] (Fig. 5a), a trend also observed at reduced catalyst loadings. MOF-containing samples exhibit similarly high oxygen release, with CO_2 and trace CO formation due to oxidation of the organic linker. Although m/z 28 corresponds to both CO and N_2, the signal remains at baseline except for a peak coincident with CO_2 evolution, suggesting that the observed m/z 28 peak change is predominantly due to CO. At 0.42 wt% Ni content, $LiClO_4$/Ni-MOF-74 generates 97.3 mol% O_2 (Fig. 5b), while $LiClO_4$/UMCM-74-I(Ni) produces 95.2 mol% O_2 (SI Fig. S7), with the remainder consisting of CO_2 and CO. The slightly lower oxygen yield reflects partial consumption of evolved O_2 during oxidation of the MOF linker.

To evaluate catalyst loading effects, mixtures of $LiClO_4$/Ni-MOF-74, $LiClO_4$/UMCM-74-I(Ni), and $LiClO_4/Ni(NO_3)_2{\cdot}6H_2O$ containing 0.21 wt% and 0.10 wt% Ni were analyzed (Table 1). As expected, reducing catalyst loading raises decomposition temperatures in all cases. These effects are most dramatic for the onset temperatures, but also substantially impact the midpoint temperatures. For example, for $LiClO_4$/Ni-MOF-74, the onset temperature increases from 317 °C to 345 °C to 419 °C as the catalyst loading drops from 0.42 to 0.21 to 0.10 wt% Ni content. The corresponding midpoint temperatures are 420 °C, 463 °C, and 478 °C. By contrast, the completion temperatures lie within a ~10 °C window. Reducing catalyst loading also slightly increases oxygen yield, with all $LiClO_4$/catalyst mixtures exceeding 97.7 and 98.8 mol% O_2 at 0.21 and 0.10 wt% Ni, respectively (SI Fig. S10–S15). Collectively, Ni-MOF-74, UMCM-74-I(Ni), and $Ni(NO_3)_2{\cdot}6H_2O$ lower the oxygen generation temperature of $LiClO_4$ while maintaining high O_2 yields; although the MOFs enable earlier O_2 release, linker oxidation slightly reduces net oxygen output relative to the nonporous salt, consistent with the expected trend of greater O_2 release at lower catalyst loadings. Nonetheless, O_2 evolution remains >95 mol% across all catalyst loadings, demonstrating that porous Ni-based MOFs are effective catalysts for lower-temperature oxygen generation.

Conclusions

Compared to conventional chemical oxygen generators, which typically rely on high-temperature decomposition of chlorate or perchlorate salts, MOF catalysts enable more facile oxygen evolution from $LiClO_4$ while preserving high O_2 purity at comparatively low catalyst loadings. The ability of the porous framework to accommodate oxidizer melt-infiltration promotes intimate nanoscale oxidizer-catalyst contact, thereby imparting catalytic effectiveness and consistently reducing oxygen release temperatures. This effect enables ~180 °C reductions in $LiClO_4$ decomposition temperature, among the largest reported temperature reductions for any catalytic system. These findings show that catalytic efficiency in oxygen-generating systems can be improved through structural design rather than solely through metal identity or loading. Notably, while porosity is critical, variation in pore size between the MOFs examined has only a modest influence on the catalytic

effect under the conditions studied and MOF linker carbon content primarily affects oxygen purity.

Conflicts of interest

There are no conflicts to declare.

Data availability

Supplementary information (SI): characterization, bimetallic catalyst study, and supporting data. See DOI: https://doi.org/10.1039/d6dt01134a.

Acknowledgements

This work was funded by the AFOSR (Grant No. FA9550-23-1-0639).

References

1 H. Kumar, P. N. Tengli, V. Kumar Mishra, P. Tripathi, A. Bhushan and P. Kumar Mishra, *RSC Adv.*, 2017, **7**, 36594–36604.
2 T. Chen, P. Du, W. Jiang, J. Liu, G. Hao, H. Gao, L. Xiao, X. Ke, F. Zhao and C. Xuan, *RSC Adv.*, 2016, **6**, 83838–83847.
3 Y. Chang, W. Zhao, E. Chu, J. Nie, W. Ren, B. Duan and Q. Jiao, *RSC Adv.*, 2025, **15**, 23867–23873.
4 S. Bekhouche, D. Trache, A. Abdelaziz, A. F. Tarchoun and H. Boukeciat, *Thermochim. Acta*, 2023, **720**, 179413.
5 A. Dey, J. Athar, P. Varma, H. Prasant, K. A. Sikder and S. Chattopadhyay, *RSC Adv.*, 2015, **5**, 1950–1960.
6 A. Fahd, C. Dubois, J. Chaouki and J. Z. Wen, *J. Therm. Anal. Calorim.*, 2022, **147**, 10245–10257.
7 P. M. Gandhi, M. Schoenitz and E. L. Dreizin, *Combust. Flame*, 2023, **249**, 112615.
8 Y. Li, H. Huang, X. Lin, R. Pan and J. Yang, *RSC Adv.*, 2016, **6**, 54310–54317.
9 T. Wu and M. R. Zachariah, *RSC Adv.*, 2019, **9**, 1831–1840.
10 W. Q. Pang, L. T. DeLuca, H. X. Xu, X. Z. Fan, F. Q. Zhao and W. X. Xie, Chemical Rocket Propulsion, in *Effects of Dual Oxidizers on the Properties of Composite Solid Rocket Propellants*, ed. L. T. De Luca, T. Shimada, V. P. Sinditskii and M. Calabro, Springer, Cham, 2017, pp. 403–423.
11 S. Gayathri and S. Reshmi, *Polym. Adv. Technol.*, 2017, **28**, 1539–1550.
12 A. Fahd, M. Y. Zorainy, C. Dubois, D. C. Boffito, J. Chaouki and J. Z. Wen, *Thermochim. Acta*, 2021, **704**, 179019.
13 E. Shafirovich, C. Zhou, S. Ekambaram, A. Varma, G. Kshirsagar and J. E. Ellison, *Ind. Eng. Chem. Res.*, 2007, **46**, 3073–3077.
14 E. Shafirovich, A. Garcia, A. K. Narayana Swamy, D. J. Mast and S. D. Hornung, *Combust. Flame*, 2012, **159**, 420–426.
15 J. Dingley, D. Williams, P. Douglas, M. Douglas and J. O. Douglas, *Anaesthesia*, 2016, **71**, 1464–1470.
16 W. Wang, L. Jin, N. Gao, J. Wang and M. Liu, *J. Chem.*, 2018, **2018**, 7469783.
17 M. A. Machado, D. A. Rodriguez, Y. Aly, M. Schoenitz, E. L. Dreizin and E. Shafirovich, *Combust. Flame*, 2014, **161**, 2708–2716.
18 N. Gao, C. Ma, K. Kariman, J. Liu, Z. Zhang, Y. Dai and Z. Wang, *J. Chem.*, 2021, **2021**, 6088484.
19 J. Liu, L. Jin, N. Gao, S. Ou, S. Wang and W. Wang, *Int. J. Miner., Metall. Mater.*, 2019, **26**, 925–937.
20 N. A. Tomalia and A. J. Matzger, *ACS Mater. Lett.*, 2025, **7**, 3035–3040.
21 N. A. Tomalia, Y. Rakova, A. N. Tubman and A. J. Matzger, *Chem. Mater.*, 2026, **38**, 2055–2062.
22 J. L. de la Fuente, *J. Propul. Power*, 2013, **29**, 293–298.
23 B. D. Hirt, C. W. Wernex, A. Sehirlioglu, M. Örnek and S. F. Son, *J. Energ. Mater.*, 2025, **43**, 636–655.
24 F. Solymosi and E. Krix, *J. Catal.*, 1962, **1**, 468–480.
25 L. Chen, L. Li and G. Li, *J. Alloys Compd.*, 2008, **464**, 532–536.
26 G. Mani, V. A. Kumar and S. Mathew, *RSC Sustainability*, 2023, **1**, 2081–2091.
27 J. Zhang, B. Jin and R. Peng, *Appl. Surf. Sci.*, 2024, **647**, 158970.
28 S. Wei, Y. Zhang, H. Tan, Z. Xia, L. Zhai, J. Hu, Q. Yang, G. Xie, Z. Chen and S. Chen, *Small*, 2024, **20**, 2400712.
29 J. Zhang, W. Chen, H. Li, F. Zhao, J. Yi, B. Jin and R. Peng, *Langmuir*, 2024, **40**, 15421–15429.
30 Y. Yang, Y. Bai, F. Zhao, E. Yao, J. Yi, C. Xuan and S. Chen, *RSC Adv.*, 2016, **6**, 67308–67314.
31 S. Wang, B. Ye, C. An, J. Wang and Q. Li, *J. Mater. Sci.*, 2019, **54**, 4928–4941.
32 J. Liu, Y. Chen, X. Zhang and Z. Ma, *J. Solid State Chem.*, 2025, **350**, 125488.
33 H. Feng, X. Liu, Y. Li, X. Ma, Q. Yan and F. Zhao, *Powder Technol.*, 2022, **397**, 117035.
34 W.-S. Dong, W.-L. Cao, Q.-N. Tariq, X.-W. Wu, Y. Hu, C. Zhang and J.-G. Zhang, *Dalton Trans.*, 2022, **51**, 9894–9904.
35 J. Li, Z. Jin, B. Jin, L. Luo and R. Peng, *Inorg. Chem.*, 2022, **61**, 17485–17493.
36 Z. Zhao, Y. Yang, X. Yu, G. Zhang, S. Li, Z. Yan, Z. Xu and X. Xiao, *Fuel*, 2026, **403**, 136147.
37 J. Zhang, B. Jin and R. Peng, *Dalton Trans.*, 2025, **54**, 16582–16592.
38 P. Zhou, S. Zhang, Z. Ren, Y. Wang, Y. Zhang and C. Huang, *Inorg. Chem. Front.*, 2022, **9**, 5195–5209.
39 Y. Hu, B. Tao, F. Shang, M. Zhou, D. Hao, R. Fan, D. Xia, Y. Yang, A. Pang and K. Lin, *Appl. Surf. Sci.*, 2020, **513**, 145849.
40 M. M. Markowitz, D. A. Boryta and H. Stewart, *Ind. Eng. Chem. Prod. Res. Dev.*, 1964, **3**, 321–330.
41 Z. K. Nikitina and V. Y. Rosolovskij, *Zh. Neorg. Khim.*, 1997, **42**, 1252–1257.
42 A. Burcat and M. Steinberg, *J. Inorg. Nucl. Chem.*, 1968, **30**, 35–39.

43 V. K. Patel and A. Gupta, *Part. Sci. Technol.*, 2021, **39**, 790–796.
44 M. M. Markowitz and D. A. Boryta, *J. Phys. Chem.*, 1965, **69**, 1114–1123.
45 Y. Zhang, K. Yan, K. Qiu, J. Liu, Y. Wang and J. Zhou, *Propellants, Explos., Pyrotech.*, 2015, **40**, 531–538.
46 Y. Zhang, K. Yan, K. Qiu, J. Liu, Y. Wang and J. Zhou, *J. Propul. Power*, 2015, **31**, 1445–1451.
47 A. Escuer, J. Mayans and M. Font-Bardia, *Inorg. Chem.*, 2016, **55**, 3161–3168.
48 S. R. Caskey, A. G. Wong-Foy and A. J. Matzger, *J. Am. Chem. Soc.*, 2008, **130**, 10870–10871.
49 W. Brockner, C. Ehrhardt and M. Gjikaj, *Thermochim. Acta*, 2007, **456**, 64–68.
50 B. Małecka, A. Łącz, E. Drożdż and A. Małecki, *J. Therm. Anal. Calorim.*, 2015, **119**, 1053–1061.